ADVANCED HEALTHCARE MATERIALS
www.advhealthmat.de

Multiscale Thermal Analysis of Gold Nanostars in 3D Tumor Spheroids: Integrating Cellular-Level Photothermal Effects and Nanothermometry via X-Ray Spectroscopy

Rosalía López-Méndez, Anastasiia Dubrova, Javier Reguera, Rául Magro, Fátima Esteban-Betegón, Ana Parente, Miguel Ángel García, Julio Camarero, Emiliano Fonda, Claire Wilhelm, Álvaro Muñoz-Noval,* and Ana Espinosa**

In the pursuit of enhancing cancer treatment efficacy while minimizing side effects, near-infrared (NIR) photothermal therapy (PTT) has emerged as a promising approach. By using photothermally active nanomaterials, PTT enables localized hyperthermia, effectively eliminating cancer cells with minimal invasiveness and toxicity. Among these nanomaterials, gold nanostars (AuNS) stand out due to their tunable plasmon resonance and efficient light absorption. This study addresses the challenge of measuring nanoscale temperatures during AuNS-mediated PTT by employing X-ray absorption spectroscopy (XAS) within 3D tumor spheroids. It also aims to investigate the heat generated at the nanoscale and the resultant biological damage observed at a larger scale, utilizing confocal microscopy to establish connections between AuNS heat generation, tissue damage, and their impacts on cellular structure. These nanoscale and microscale thermal effects have been compared with macroscopic values obtained from infrared thermography, as part of a multiscale thermal analysis. The findings underscore the efficacy of AuNS in enhancing PTT and provide insights into the spatial distribution of thermal effects within tumor tissues. This research advances the understanding of localized hyperthermia in cancer therapy and underscores the potential of AuNS-based PTT for clinical applications.

1. Introduction

In the quest to address the complexities of cancer and mitigating the risks associated with current treatment modalities, efforts have increasingly focused on enhancing therapeutic efficacy while minimizing safety concerns. Near-infrared (NIR) photothermal therapy (PTT), employing photothermally active nanomaterials, is emerging as a pivotal approach in tumor treatment.[1,2] This method entails the application of highly localized tissue heating, inducing hyperthermia that effectively destroys cancer cells through light-to-heat conversion. This strategy offers inherent advantages, including noninvasiveness, minimal toxicity, increased selectivity, and reduced potential for initiating resistance. Various nanoplatforms have been identified, spanning different compositions, shapes, and structures of metal nanoparticles, including gold and silver,[3–5] carbon nanomaterials and dots,[6–8] graphene

R. López-Méndez, J. Camarero, Á. Muñoz-Noval
IMDEA Nanociencia
c/Faraday, 9, Madrid 28049, Spain
A. Dubrova, C. Wilhelm
Laboratoire Physico Chimie Curie
PCC
CNRS UMR168
Institut Curie
Sorbonne University
PSL University
Paris 75005, France
E-mail: claire.wilhelm@curie.fr

The ORCID identification number(s) for the author(s) of this article can be found under https://doi.org/10.1002/adhm.202403799

DOI: 10.1002/adhm.202403799

J. Reguera
BCMaterials, Basque Center Centre for Materials Applications and Nanostructures
UPV/EHU Science Park, Leioa 48940, Spain
J. Reguera
Departamento de Física de la Materia Condensada – GIR Bioforge
Universidad de Valladolid
edificio LUCIA, paseo de Belén 19, Valladolid 47011, Spain
R. Magro, F. Esteban-Betegón, A. Espinosa
Instituto de Ciencia de Materiales de Madrid
ICMM-CSIC
c/ Sor Juana Inés de la Cruz, 3, Madrid 28049, Spain
E-mail: ana.espinosa@csic.es
A. Parente, Á. Muñoz-Noval
Dpto. Física Materiales
Facultad CC. Físicas
Universidad Complutense de Madrid
Madrid 28040, Spain
E-mail: almuno06@ucm.es

oxide,[9] and other inorganic nanoparticles such as silver sulfide,[10] copper sulfide,[11,12] iron oxide[13,14] or MXenes.[15] Among these, NIR-absorbing Au nanomaterials, encompassing Au nanoshells,[16,17] Au nanorods,[18,19] Au nanocages,[20] hollow Au nanospheres,[21,22] and Au nanostars, have emerged as the most prominent and widely studied nanoparticle types. Among the aforementioned NIR-induced gold-based nanoplatforms, Au nanostars (AuNS) stand out as particularly effective for applications in optical biosensing, imaging, and PTT.[23–27] This is largely attributed to their branched morphology which enables high plasmonic resonance within the NIR spectrum, all while maintaining a small nanoparticle size in the 25–75 nm range.[28,29] In contrast, prototype Au nanoshells have diameters typically exceeding 150 nm.[30] One notable feature of AuNSs is their impressive ability to finely tune their localized plasmon resonance spectra and enhance their light absorption efficiency by adjusting parameters like width, length, and spike count.[28,31] Modifying the number and aspect ratio of spikes can be easily accomplished by adjusting the concentration of $HAuCl_4$ and shape-directing agents in the seed-mediated growth process of their chemical synthesis.[27–29] Furthermore, AuNSs facilitate seamless conjugation with a diverse array of bioactive and cancer-targeting agents, thereby paving the way for combination therapies such as PTT alongside drug delivery[32–34] or photodynamic therapy (PDT).[35–37] All this makes it a versatile and effective state-of-the-art PTT agent. Moreover, when internalized by cancer cells and confined in endosomes, even small particles (≈25 nm) exhibit significant absorption in the NIR spectrum due to plasmon coupling between neighboring nanostars.[27,38]

One of the challenges in PTT lies in achieving accurate and precise temperature measurements at the nanoscale within tissues undergoing photothermal treatments. This entails the development of nanothermometric techniques capable of effectively sensing temperature changes in response to localized heating. It also involves addressing factors such as high resolution and the dynamic biological environment. Furthermore, ensuring the compatibility of these nanothermometers with photothermal agents and the targeted cells or tissues introduces complexity to the design and implementation of reliable nanothermometry techniques for hyperthermia. In response to these essential demands for thermal sensing within cellular and tissue contexts, a diverse array of nanothermometers has been created. These solutions harness the potential of luminescent nanoparticles,[39] fluorescent organic dyes,[40] quantum dots,[41,42] nanodiamonds,[43] thermosensitive polymers,[44,45] and metallic nanoparticles.[46] These nanoprobes enable precise temperature measurements within tissue environments and can serve as intracellular temperature indicators for processes involving thermogenesis or thermal therapies. Additionally, nanoscale photothermal effects can be investigated using a recent nanothermometric methodology using X-ray absorption spectroscopy (XAS).[47–49] Gold-iron oxide nanoparticles activated by NIR light exhibited a significantly elevated local heating at the nanoparticle scale both in solid solutions and in tumor cells using this nanothermal method[48,49] compared with overall temperature. Raising the temperature significantly leads to physical harm, including protein denaturation and membrane rupture. This process can elevate oxidative stress, ultimately resulting in coagulative necrosis or apoptosis. These effects are expected to be even more pronounced in the vicinity of nanoparticles, as they are confined within endosomes inside cells.

Due to the significant plasmon-induced thermal gradient observed at the nanoscale within tissue environment,[49] a key concern in PTT treatments is to establish the relationship between induced thermal damage and its spatial extent around the activated heating sources in tumor tissues. Consequently, understanding the biological effects of the localized heat generated in tumor tissues at cellular level still requires further investigation. In this context, 3D tumor models are now preferred for pre-clinical assessment of anti-cancer treatments, striking a balance between the lack of microenvironment in adherent cell cultures and the complexity of in vivo animal models. In spheroids, cancer cells grow as aggregates, promoting cellular proliferation and stimulating extracellular matrix (ECM) production, thereby enhancing cell-cell contact and communication.[50,51] Moreover, the heat produced by thermoexcited nanoparticles within tightly packed cells is not dissipated as rapidly as in 2D cell cultures due to the spheroids' high surface-to-volume ratio, providing a more realistic representation of a heated tumor environment.[50,52–55] The 3D model thus combines features such as coupled capillary and interstitial heat transfer and transport, which are the fundamental mechanisms governing the distribution of heat in nano-based hyperthermic treatments.[56]

Another major challenge lies in fine evaluation of local nanoparticles' hyperthermic effect and resulting cellular tissue damage. To date, confocal microscopy provides one of the most advanced and convenient techniques to precisely evaluate nanoscale impact in live and fixed tissues. It allows for the tracking of temperature changes and thermal damage, including alterations in membrane integrity and protein denaturation, with high-resolution in 3D. Fluorescent probes may serve as optical microprobes to not only assess cell viability post-treatment but gain insight into cellular organization and its associated functions. As such, staining actin filaments that comprise part of the cell cytoskeleton responsible for cell movement can relate to cancer migration, as microfilament disruption has been shown to be associated with its inhibition.[57] In addition, a plethora of cell-cell adhesion complexes, which serve as associated tumor markers, can be observed to assess the potential effect of local hyperthermia on cancer cells. Among those, the cadherin super-

M. Ángel García
Departamento de Electrocerámica
Instituto de Cerámica y Vidrio
ICV-CSIC
Kelsen 5, Madrid 28049, Spain
J. Camarero
Departamento de Física de la Materia Condensada and Instituto 'Nicolás Cabrera'
Universidad Autónoma de Madrid
Madrid 28049, Spain
E. Fonda
Synchrotron SOLEIL
L'Orme des Merisiers – St. Aubin-BP 48
Gif s/Yvette 91192, France
A. Espinosa
Unidad de Nanomateriales Avanzados
IMDEA Nanociencia, Unidad Asociada al CSIC por el ICMM
c/ Faraday 9, Madrid 28049, Spain

family of adherent junctions, and more specifically E-cadherin, is one of the most explored proteins so far, indicative of tissue epitheliality.[58] Therefore, its observed loss or gain following the nanoparticle-localized hyperthermal effect may reveal the respective changes in tissue integrity and hence, its metastatic potential.[59] Targeted visualization of such crucial proteins with confocal microscopy may allow to further detail the extent and distribution of hyperthermic damage and thus, providing insights into the overall efficacy and safety of nanoparticle-based therapies.

This study employs an X-ray spectroscopy-based approach to measure the photothermal heating generated by AuNS within 3D cancer spheroids. Additionally, it explores cellular damage on a larger scale through microscopic analysis of thermal effects and their spatial distribution around activated heating sources. The aim is to establish connections between heat generation, tissue damage, and their effects on cellular structure. Our findings demonstrate that localized temperatures achieved at the nanoscale can exceed those measured at the macroscopic scale, revealing a critical thermal threshold that may indicate the breakdown of cell-cell adhesion. This research emphasizes the importance of accurately assessing nanoscale heating effects to guide the design of more effective photothermal therapies that maximize damage to cancer cells while minimizing harm to healthy tissues.

2. Results

2.1. Characterization of Gold Nanostars in 3D Tumor Spheroids

Gold nanostars (AuNS) were synthesized using seed-mediated protocol following established procedures, employing the polyvinylpyrrolidone/dimethylformamide (PVP/DMF) route synthesis, resulting in a core with a branched structure.[27,28] **Figure 1A** displays representative transmission electron microscopy (TEM) images of AuNS. More TEM images are shown in Figure S1 (Supporting Information). Regarding their optical properties, AuNS exhibited localized surface plasmon resonances (LSPR) within the visible to near-infrared (Vis-NIR) region with a broad band in the 600–900 nm range and a maximum at 735 nm, which is attributed to a tips-core hybridized plasmon mode (see Figure 1B) and a small band in the 500–600 nm region attributed to the core plasmon mode. X-ray diffraction (XRD) patterns, as presented in Figure 1C (upper panel), further confirmed the presence of a crystalline face-centered cubic (fcc) metallic Au phase.

AuNS were incubated with U87 glioblastoma cancer cells for 24 h at an extracellular Au concentration ranging from 12.5 to 100 μM. Figure 1D illustrates the internalization of AuNS with a 58.0 ± 1.4 nm average equivalent diameter (Figure 1E) within cells through TEM, clearly showing the sequestration of these nanoparticles within endosomes, indicating an endocytosis-mediated pathway. The cytotoxicity assessment performed revealed that the AuNS were biocompatible under these incubation conditions (Figure 1F), with cellular uptake ranging from 0.3 to 9.8 pg cell^{-1} of Au (Figure 1G). U87, a glioblastoma cell line representing brain cancer, was employed as a model system to generate aggregates, primarily in the form of spheroids, to replicate the characteristics of tumor tissue. 3D spheroid models not only replicate the complex microenvironment within solid tumors and mimic various tumor characteristics but also facilitate the simulation of a realistic heated tumor mass, accounting for subsequent heat exchange and environmental losses. U87 cells were initially labeled with AuNS at a concentration of 200 μM of Au. Subsequently, ≈300,000 cells were collected to form spheroids. Histological analysis was employed to assess the viability of spheroid-forming cells (Figure 1H). Hematoxylin and eosin-stained histological sections demonstrated viable and compact tissue in labeled cells.

AuNS exhibit a red-shift of the extinction band, moving the peak of their LSPR from 735 to 796 nm due to plasmonic coupling.[27,38] This extends their absorption capability into the broader NIR-I and NIR-II regions. Advanced high brightness X-ray diffraction (XRD) spectroscopy revealed that AuNS inside the cell aggregates exhibit patterns typical of fcc metallic Au (Figure 1C), along with crystals of physiological salts formed within the cells. These findings indicate that AuNS remained unchanged after exposure to the cellular environment, retaining their star-like architecture and crystalline composition.

U87 cells with AuNS formed a compact and homogeneous tumor spheroid of ≈ 300 μm in diameter (Figure 1I). High-resolution confocal microscopy imaging of live/dead assay staining of spheroids revealed maintained high viability of individual cells comprising the aggregates. Confocal immunofluorescence images (Figure 1J) show the structure of the spheroids, including the cell cytoskeleton (actin network) and cell-cell adhesion patterns (E-cadherin). The strengthened E-cadherin bonds indicate the cohesiveness and integrity of the tissue. The 3D spheroid integrity and toxicity of U87 cells were not affected by the presence of internalized AuNS.

2.2. Nanoscale Thermal Probing Inside Cells using X-Ray Absorption Spectroscopy (XAS)

Recent findings have shown that extended X-ray absorption fine structure (EXAFS) spectroscopy can accurately detect local heating in diverse inductively thermal systems.[47,48,60] More recently, we have introduced in situ EXAFS spectroscopy as a precise, versatile, and direct nanothermometric technique at the cellular level within the tumor environment.[49] This approach relies on analyzing the vibrations of structural parameters of heated atoms, such as Au in this case, inferred from fitting the structural Debye-Waller (DW) factor extracted by the EXAFS signal $\chi(k)$ with temperature from a previous study:

$$\chi(k) = \sum_i \frac{\left(N_i S_0^2\right) F_i(k)}{k R_i^2} \sin\left[2kR_i + \delta_i(k)\right] e^{-2\sigma_i^2 k^2} e^{-2R_i/\lambda(k)} \quad (1)$$

where N_i represents the coordination number of atom i, R_i denotes the interatomic distance of each shell, and σ_i^2 is the mean displacement due to thermal motion (DW factor). This factor quantifies the thermal vibrations of atoms and can be modeled according to a correlated Debye model equation. See Supporting Information for more details. At high temperatures, this factor can be expressed as:

$$\sigma_T^2 \approx \frac{A}{\theta_D}\left(\frac{1}{4} + \frac{T}{\theta_D}\right) \quad (2)$$

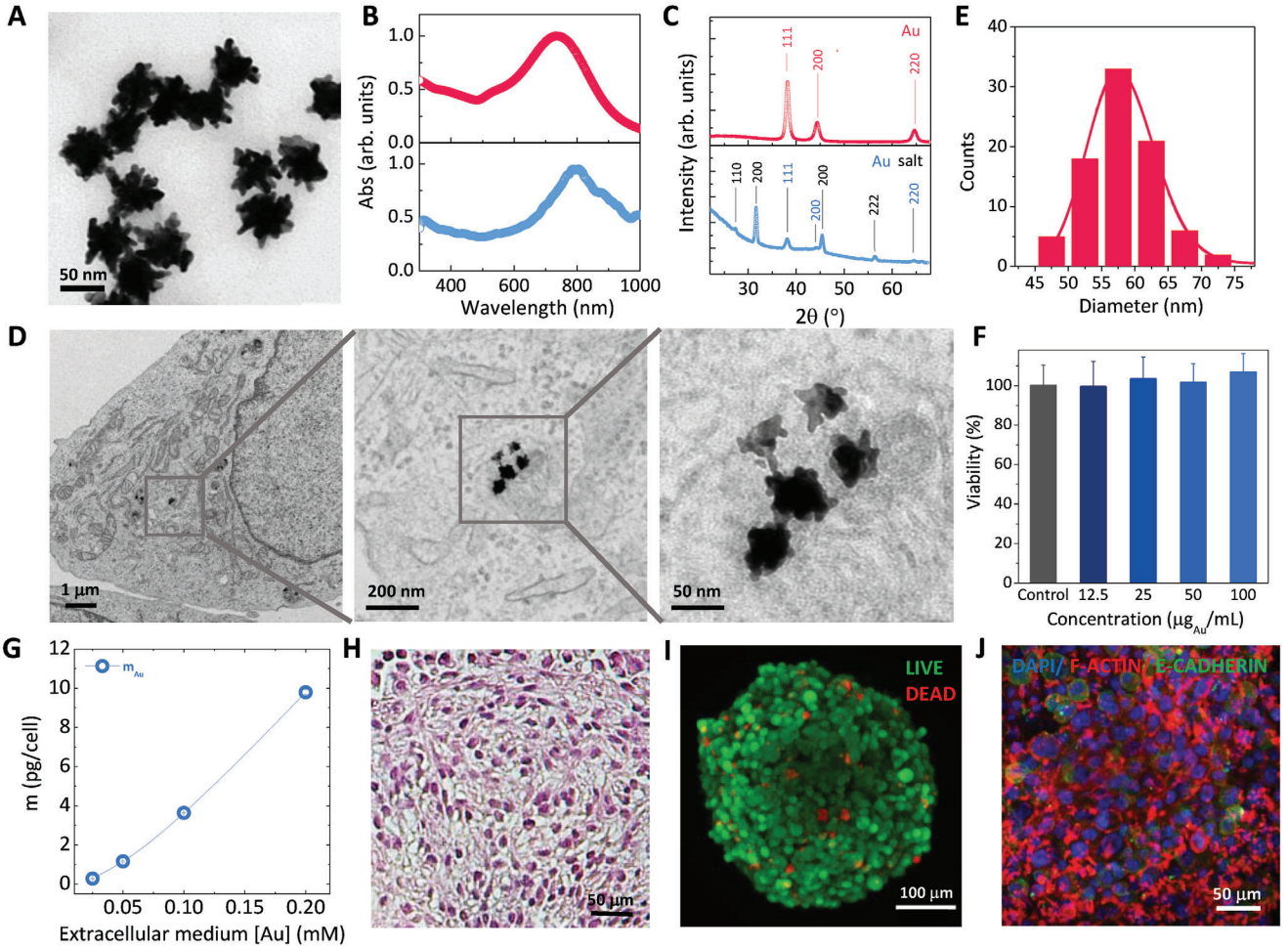

Figure 1. A) TEM image of AuNS (with a diameter of 58.0 ± 1.4 nm). B) UV–Vis–NIR spectra of AuNS in solution (on top) and inside U87 glioblastoma cells (down), both reveal the presence of a plasmon resonance in the near-infrared (NIR) region. C) X-ray diffraction (XRD) pattern of AuNS in solution (on top) and inside U87 cells (down). D) TEM micrographs of AuNS in U87 cells. E) Particle size distribution analysis of the AuNS in water. F) Cell viability of AuNS assessed in U87 cells after 24 h of exposure to different extracellular concentrations (12.5, 25, 50, and 100 µg$_{Au}$ ml^{-1}). G) Cellular internalization of AuNS quantified using inductively coupled plasma optical emission spectroscopy (ICP-OES) in mass of Au per cell after a 24-h incubation at extracellular concentrations ranging from 25 to 200 µM. H) Hematoxylin and eosin staining of a labeled spheroid section. I) 3D reconstructed confocal images of live/dead cells in the formed spheroid with AuNS. Green fluorescent calcein indicates live cells, while red component, iodide, marks dead cells. J) 3D reconstructed confocal images of a spheroid with AuNS stained with F-actin (cytoskeleton, red), E-cadherin (cell junctions, green), and DAPI (nuclei, blue).

where A is a constant containing the reduced mass $M = \frac{m_1 * m_2}{m_1 + m_2}$ of the atom pair, k_B the Boltzmann constant, $\hbar$ is Planck's constant, and θ_D the Debye-Einstein temperature ($A = \frac{3\hbar^2}{Mk_B}$).

XAS measurements were conducted on the SAMBA beamline (SOLEIL synchrotron, France) at the Au L_3-edge in fluorescence mode due to the absorption properties of cell tissue. This method ensures precise and reliable data acquisition, essential for characterizing the local structural and electronic properties of the AuNS in their biological environment. The X-ray absorption near-edge structure (XANES) analysis revealed the electronic structures of metallic Au within cellular environments (**Figure 2**A). The results were benchmarked against reference samples of bulk metallic Au (Au foil) to ensure accuracy. The data confirmed the preservation of the AuNS electronic properties after cellular uptake, demonstrating the stability and integrity of these nanomaterials in biological settings.

A calibration temperature experiment ranging from 100 to 350 K using a helium gas exchange cryostat was first conducted to determine the thermal dependency of σ_i^2 for Au atoms. Two distinct temperature ranges were examined: from 100 to 300 K, with increments of 60–70 K, and above 300 K, with intervals reduced to 25 K to achieve greater precision. The EXAFS signal amplitude is impacted by the thermal motion of atoms as shown in Figure 2B. Fourier transform (FT) of the k^2-weighted EXAFS signals of AuNS within cells is displayed in Figure 2C (non phase-corrected), across various temperatures, using a k-range of 2.5 to 11 Å^{-1}. It shows two main peaks associated with the metallic Au-Au bond distances ($R_{Au\text{-}Au}$ = 2.86 Å and assuming a mean coordination number N = 12 for Au metallic bulk). The FT of the

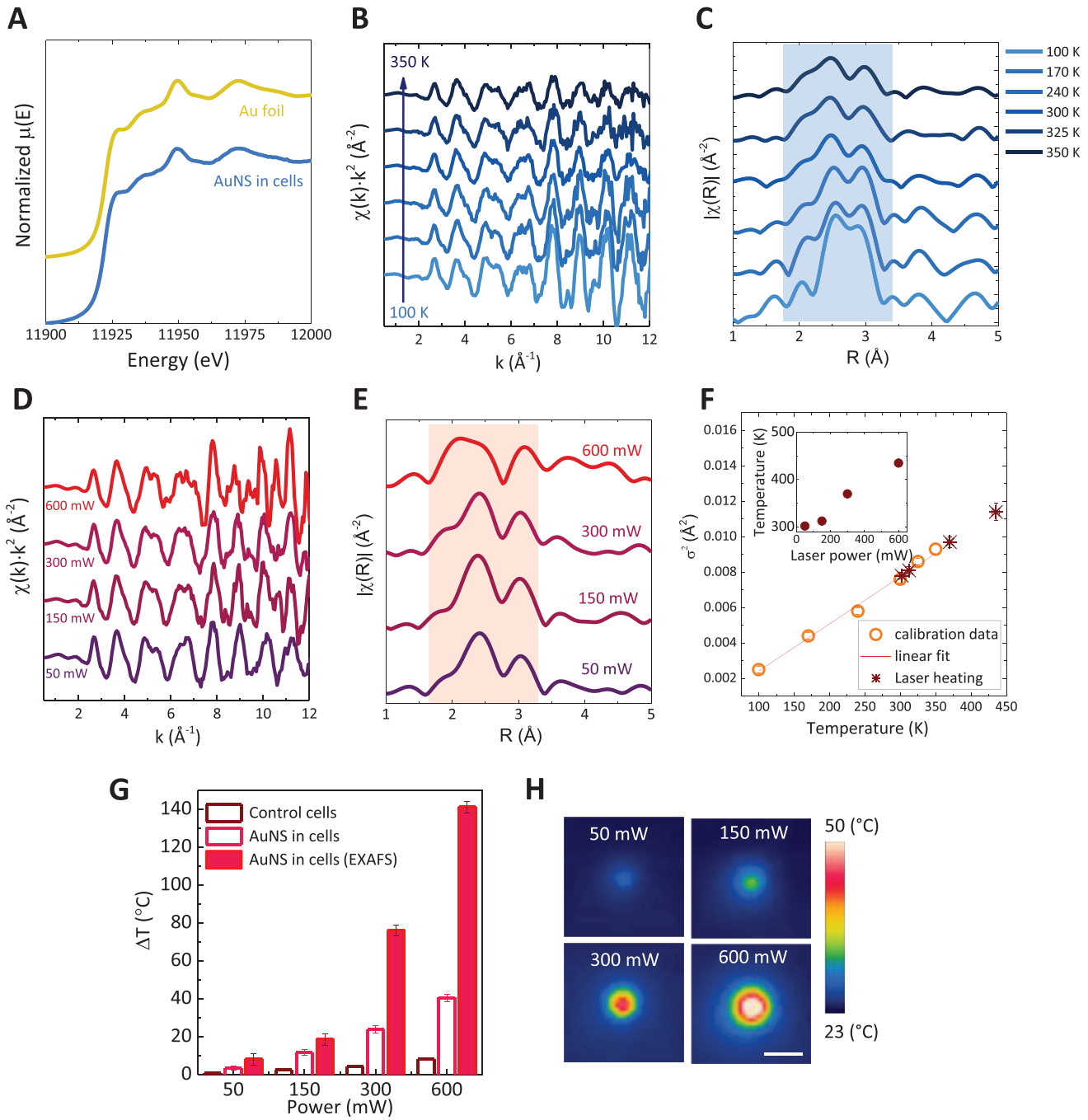

Figure 2. A) X-ray absorption near-edge structure (XANES) at Au L_3-edge (11919 eV) of AuNS in cells compared with Au foil reference at 300 K. Temperature evolution of the B) EXAFS oscillations (k^2-weighted) and C) Fourier Transform (FT) EXAFS signal extracted from Au L_3-edge XAS spectra measured from 100 to 350 K. D) Au L_3-edge EXAFS oscillation functions (k^2-weighted) subjected to photothermal irradiation at different laser powers (0.05–0.6 W). E) FT EXAFS signal under photothermia (0.05–0.6 W). F) Calibration curve of the DW as a function of temperature for AuNS (open symbols). Solid symbols represent calculated values under photothermal excitation. Solid lines depict the fitting based on the Debye-Einstein model in the linear approximation (100–350 K). The inset shows the local temperatures achieved under laser excitation (0.05–0.6 W). G) Average temperature increases of AuNS in cells subjected to various laser powers using EXAFS analysis (local temperature) and an infrared thermal camera (macroscopic). Average temperature elevation of control (unlabeled) cells was also measured under laser excitation. H) Infrared thermal images of AuNS in cells under different laser powers (scale bar: 5 mm).

Table 1. Calibration of AuNS with temperature. Experimental structural parameters, such as coordination number (*N*), average Au–Au bond length (*R*), and the EXAFS Debye–Waller factor (σ^2)) derived from the EXAFS data of the AuNS under different temperatures (K) using a cryostat.

Cryostat temperature (K)	N	R [Å)]	σ^2[Å^2)]
100	10.3 (5)	2.86 (1)	0.0025 (2)
170	10.3 (5)	2.86 (1)	0.0044 (2)
240	10.3 (5)	2.86 (1)	0.0058 (2)
300	10.3 (5)	2.86 (1)	0.0076 (2)
325	10.3 (5)	2.86 (1)	0.0086 (2)
350	10.3 (5)	2.85 (1)	0.0093 (3)

k^2-weighted EXAFS spectra were fitted using theoretical phase and amplitude generated by the FEFF8.1 program[61] and analysis calculations were performed employing Artemis software.[62] The Au–Au nearest-neighbor coordination numbers for AuNS (N = 10.3) are lower than the expected for bulk fcc Au, due to the high surface-to-volume ratio. Analyzing the FT data across various temperatures enabled the determination of σ^2 and facilitated a linear calibration of the temperature-dependent structural parameters for Au atoms (refer to **Table 1**).

For comparison, Figure S2 (Supporting Information) shows that XANES and EXAFS measurements of AuNS synthesized at 300 K confirm the structural presence of fcc Au.

The DW factor calibration with temperature can effectively monitor variations in AuNS temperatures. Subsequently, AuNS in spheroids were subjected to 808 nm laser excitation (with powers ranging from 0.05 to 0.6 W), and identical measurements were conducted to assess the local temperature rise due to photoexcited hyperthermia. Additionally, an infrared thermal camera, positioned in the same setup as used for EXAFS measurements, monitored the macroscopic heating of AuNS in cells over time and with varying laser power. EXAFS spectra and extracted FT were obtained for each laser power as seen in Figure 2D,E. EXAFS fitting parameters and σ^2 values (**Table 2**) were obtained to derive local temperatures based on Au–Au first shell σ^2 values (Figure 2F) from a linear fitting equation (equation S1). Local temperatures ranged from 302 to 435 K under laser powers of 0.05 W to 0.6 W, corresponding to temperature increases (ΔT_{LOCAL}) from 8 to 141 °C (Table 2). Global temperature (ΔT_{GLOBAL}) acquired curves as a function of irradiation time are depicted in Figure S3 (Supporting Information). A comparison of ΔT_{LOCAL} and ΔT_{GLOBAL}, along with the temperature increase in control cells, is depicted in Figure 2G, indicating local thermal increments of 2–3 fold. Thermographic images of global increments are shown in Figure 2H.

Table 2. Experimental structural parameters, such as coordination number (*N*), average Au–Au bond length (*R*), and the EXAFS Debye–Waller factor (σ^2)) derived from the EXAFS data of the AuNS under laser illumination and the obtained local temperatures (T_{LOCAL} (K) and ΔT_{LOCAL} (°C)).

Laser power (mW)	Shell	N	R (Å)	σ^2[Å^2)]	T_{LOCAL} [K]	ΔT_{LOCAL} [°C]
50	Au-Au	10.3 (3)	2.86 (1)	0.0078 (2)	302 (3)	8 (3)
150	Au-Au	10.3 (3)	2.86 (1)	0.0081 (2)	312 (3)	18 (3)
300	Au-Au	10.3 (3)	2.85 (1)	0.0097 (3)	370 (3)	76 (3)
600	Au-Au	10.3 (3)	2.84 (1)	0.0114 (5)	435 (5)	141 (5)

2.3. Localization of Cancer Cell Damage Following Photothermal Treatment using Gold Nanostars in a Tumor Spheroid Model

The 3D multicellular spheroid stands out as a valuable tool for nanotoxicity evaluation and serves as a good model to monitor thermal damage at the cellular level following photothermal treatment in hyperthermic cell-based assays. The same AuNS-labeled spheroids were exposed to various photothermal doses, and 2 h after the treatment live/dead assay was performed and imaged with confocal microscopy, depicting live (green-colored) and dead (red-colored) cells as shown in **Figure 3A**. Observations of heat-induced cell death analysis have shown that increasing thermal doses result in the destabilization (starting from 150 mW, ΔT_{LOCAL} = 18.5 °C) and disintegration of the spheroid, leaving few to no surviving cells at doses ranging from 300 to 600 mW (ΔT_{LOCAL} above 75 °C). The metabolic activity in cell aggregates was assessed using a colorimetric assay with the Alamar Blue reagent (Figure 3B). A clear change in the overall metabolic health and viability of the cell aggregates was detected under 150 mW laser irradiation, with almost no metabolic activity observed at higher laser power doses. This result is in agreement with the percentage of live cells quantified from Figure 3A (see Figure S4, Supporting Information).

To further investigate the impact of local nanoparticle hyperthermia at a finer level of cell structure, spheroids subjected to variable doses of laser power were also fixed following the treatment for subsequent immunostaining. Namely, the changes induced with cell cytoskeleton as well as cell-cell junctions were traced via F-actin and E-cadherin staining, respectively (Figure 3C). As such, F-actin staining revealed that for higher doses of laser power (150 – 300 mW) the hyperthermal treatment induced progressive cytoskeleton damage with little-to-no observable F-actin at the highest laser power of 300 mW. This may be an indicator of cytoskeleton collapse events that, in turn, have been shown to be associated with inhibited cell migration and vast impairing of other cellular functions.[57,63,64] Such an outcome may be beneficial for therapeutic applications in the context of cancer metastasis. On the other hand, we observed an increase in E-cadherin protein fluorescence at 150 and 300 mW laser dosages as compared to the lower laser power, 50 mW, and untreated control. This not only demonstrates that cancer cells did not lose their cell-cell junctions and acquiring a more metastatic phenotype but also suggests a potential stimulation in intercellular adhesions via local hyperthermal treatment. Tumor spheroid cells were also monitored using TEM imaging to investigate potential photothermal-induced AuNS degradation within cells under different thermal doses (Figure 3D). Surprisingly, nanostars were successfully visualized as intact and internalized within cells in spheroids even post higher laser exposure dose (see Figure S5, Supporting Information). This indicates the absence of detrimental impact of photothermal irradiation on either the morphology or integrity of AuNS inside cancer cells, even at 300 mW where nanoparticle spikes are still preserved.

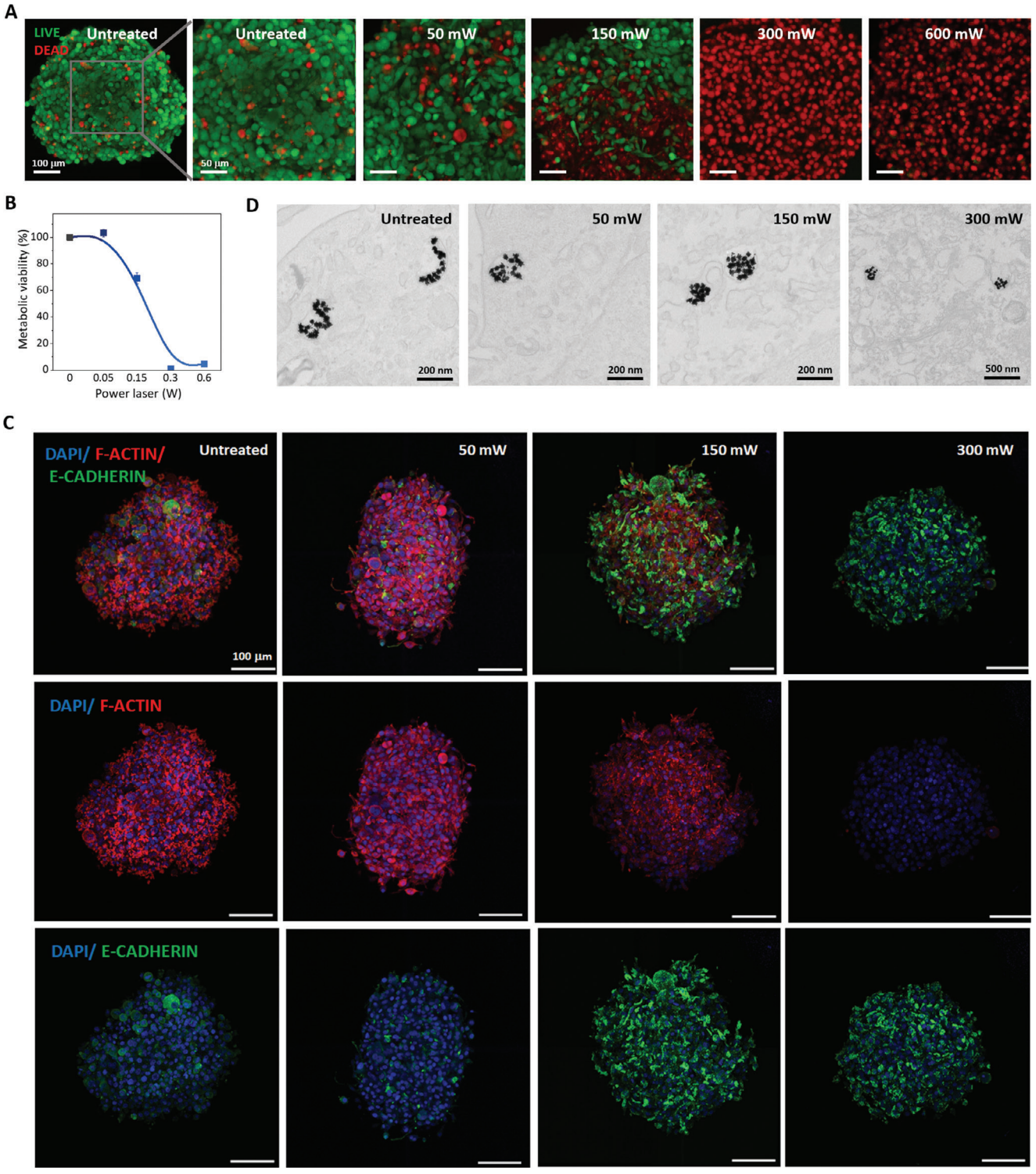

Figure 3. Microscale thermal characterization of spheroids under photothermal effects with microscopy techniques. A) Confocal fluorescence imaging of 3D spheroids labeled with AuNS treated at different photothermal doses (0.05–0.6 W) and stained with Live/Dead solution. B) Metabolic activity in cell spheroids was determined using a colorimetric assay (Alamar Blue). C) 3D rescontructed confocal images of a single spheroid with AuNS stained with F-actin (cytoskeleton, red), E-cadherin (cell juntions, green) and DAPI (nucleus, blue). D) TEM imaging analysis of AuNS internalization inside cells localized in endosomes after photothermal treatments.

3. Discussion

This study successfully demonstrates the integration of high photothermally efficient AuNS into a 3D tumor spheroid model derived from U87 glioblastoma cells. AuNS preserved their crystalline structure, as evidenced by TEM images and XRD, even after cellular uptake, indicating their stability within the biological environment. High cancer spheroid cell viability, cytoskeleton stability, and overall adherent junction integrity, demonstrated via live/dead assays as well as E-cadherin and F-actin protein expression, establish a robust control framework for further photothermal irradiation studies. Similar results in the presence of AuNS within tumor spheroids further underscore their non-toxic nature in 3D cultures—a crucial consideration for potential therapeutic application.

The study explores the potential of state-of-the-art AuNS as both photothermal agents and nanothermometric probes using intracellular XAS. By employing EXAFS analysis, the study demonstrates the ability to monitor local temperature variations at the nanoscale within the tumor spheroid environment during photothermal treatments. Calibrating the Debye-Waller factor (DW) with temperature allows for precise determination of local temperatures, with increases ranging from 13 to 28% in the 300 to 350 K range. The linear response of DW to these temperatures underscores its effectiveness in detecting photoinduced heating in AuNS. The analysis reveals parameter differences in σ^2 up to 25 – 47% under exposure at the highest laser powers. The temperature-dependent EXAFS data provide valuable insights into the thermal behavior of AuNS under various laser powers, offering a detailed framework for assessing photothermal effects in a controlled and quantifiable manner. Moreover, this nanothermometric technique proves reliable and robust in the cellular environment: EXAFS remains stable regardless of concentration and is resilient to changes in pH and viscosity.

As previously observed, gold-based nanomaterials under photoexcitation generate thermal gradients around them.[48] When these nanoparticles are embedded in the cellular matrix, heating is notably amplified, resulting in local temperatures that are significantly higher than global temperature measurements.[49] Specifically, under laser exposure, the local temperatures generated by AuNS in cells are ≈2 to 3 times higher than those recorded macroscopically. This finding aligns with previous experimental and theoretical studies on nanoparticles subjected to magneto- or photo-thermal heating modalities in solution.[44,45,65–68] It is important to note that compared to similar spiky gold-based nanomaterials combined with iron oxide as a hybrid, the thermal gradient is less pronounced in AuNS alone in cells. The iron oxide in hybrid systems acts as a thermal reservoir, moderating the dissipation of the heat generated by the plasmonic gold nanoparticles. While iron oxide (in the form of magnetite) also absorbs NIR light and emits heat, it does so less effectively than the heat produced by the LSPR of Au nanoparticles.[13,14] Various studies have documented large thermal gradients using different nanosystems, highlighting significant temperature variations within small volumes.

The integration of AuNS into the 3D spheroid model also facilitates the in-depth evaluation of photothermal-induced damage at the cellular and subcellular levels and enables correlation with the obtained nanoscale temperature results. Confocal fluorescence imaging and metabolic activity assays reveal a clear correlation between laser power and cell viability, with higher powers leading to an increased cell death and spheroid disintegration. Importantly, the structural integrity of AuNS is maintained even after photothermal treatment, as confirmed by TEM analysis, indicating their resilience and suitability for repeated therapeutic cycles. PTT also has shown to induce cell structural changes, namely, in the cell cytoskeleton (F-actin) and cellular adhesion (E-cadherin) proteins' expression. Adherent junctions and cell cytoskeleton are crucial for tissue integrity and organization preservation with major roles in cell motility, migration, intercellular signaling etc.[58,69] Numerous evidence of these cellular constituents and their functions being involved in cancer cell metastasis has already been brought to attention.[70,72] Nanomaterials-based strategies have been gaining interest over the past years as active actin inhibitors to impede cell migration, with several approaches including nanoparticle-coupled hyperthermal treatments.[73–75] Liu et al. have shown one of the latest achievements via blocking the cancer cell migration through actin cytoskeleton-linked protein targeting with the combination of gold nanorods with mild PTT.[57] Our findings correlate the extent of the thermal gradient generated in the vicinity of nanoparticles with its propagation at different scales, depending on photothermal excitation conditions, and with subtle changes in actin filament organization and cadherin-mediated adhesion. These changes suggest a promising impact on tumorigenesis by disrupting actin filament networks while preserving crucial cell-cell adhesions. In this work, we have demonstrated the potential effects of AuNS-targeted PTT on the cell cytoskeleton and intercellular junctions. When combined with highly precise local measurements of photothermal treatment effect propagation, this approach will allow us to further study the modulation of nanoparticle photothermia response in cancer cells at the subcellular level and its implications for therapeutic applications. Among the various parameters that can be monitored to evaluate cell integrity and the cytoskeleton, we have selected the most representative and fluorescently brilliant indicators.

4. Conclusion

This study offers a thorough evaluation of AuNS as both photothermal agents and nanothermometric probes using XAS. The linear relationship observed between the Debye-Waller factor and temperature demonstrated the sensitivity of AuNS in detecting photoinduced heating, with temperature measurement uncertainties ≈ 3–5°C, and revealed significant photothermal gradients within the cellular environment. Indeed, the local temperatures measured at the nanoscale around AuNS were higher than global temperature measurements, highlighting substantial thermal gradients. Besides, compared to hybrid nanomaterials, AuNS exhibit a relatively lower thermal gradient, suggesting more controlled and localized heating effects. Importantly, the study confirms that AuNS remain intact within cells, with no apparent thermal degradation, making them reliable for prolonged use in therapeutic applications. The research highlights their dual role as effective photothermal agents and precise temperature sensors in controlled cancer treatment applications.

This work also establishes a clear connection between nanothermally induced effects and cellular damage. It demonstrates

how varying irradiation doses influence overall cell-cell interactions, cellular structure, and integrity at the cellular scale. Higher laser powers were found to increase cell death and spheroid breakdown, reflecting the thermal effects around the nanoparticles, while lower hyperthermia conditions enhanced cellular response.

Overall, this study represents the pioneering detailed investigation into the multiscale thermal effects of AuNS, examining their nanospatial extent around activated heating sources in tumor tissues and their impact on cellular structure and viability. By elucidating the interplay between nanoscale heating and cellular responses, this study contributes to the broader field of nanomedicine and holds promise for developing innovative strategies in targeted cancer therapies.

5. Experimental Section

Gold Nanostar Synthesis: Gold nanostars were synthesized by a seed-mediated-growth method. Initial gold seeds of ≈14 nm were synthesized by a modified Turkevith method: 95 mL of 0.5 mM $HAuCl_4$ in ultrapure water was heated and brought to boil. Then, 5 mL of 1 wt. % of sodium citrate tribasic dihydrate was quickly added under strong stirring and left to react for 15 min. After that, the sample was cooled down and stored in the fridge until further use.

The seed solution was taken from the fridge and left stirring until it reached room temperature. The Au concentration of the seeds solution was measured in a UV–vis spectrometer using an extinction coefficient of 2.4 mM^{-1} cm^{-1} at a wavelength of 400 nm. A solution of PVP (MW 10 Kg mol^{-1}) was prepared at 1 mg mL^{-1} in ultrapure water. The amount of PVP added to the solution was calculated to be 60 molecules per nm^2 of nanoparticle surface. The PVP solution was added dropwise to the nanoparticle solution under mild stirring. The solution was left stirring for 1 h, and then centrifuged and redispersed in water two times. The final concentration was measured by UV–V is spectrophotometry.

For the synthesis of nanostars, 75 g of PVP (MW 10 Kg mol^{-1}) was dissolved in 1.5 L of DMF in an Erlenmeyer flask. Once dissolved, 8.19 mL of $HAuCl_4$ 50 mM in water was added and left to pre-reduce until all gold passed to Au^+, in this case during 5 min.[28] The seed solution (11.3 10^{-3} mmols of Au) was then quickly added and left for reaction for 2 h. The solution was centrifuged and the supernatant was discarded. The solution was further purified by centrifugation 3 times in ethanol and finally resuspended in ultrapure water.

Cell Culture, Nanoparticle Incubation, and Spheroid Formation: U87 human glioblastoma cells were cultivated in Dulbecco's Modified Eagle Medium (DMEM) supplemented with 10% fetal bovine serum and 1% penicillin-streptomycin at 37 °C in an incubator with 5% CO_2. When they reached high confluence, the cells were cultured in a supplemented DMEM medium for 24 h with varying concentrations of nanoparticle suspensions in T75 flasks. The concentrations of Au in the extracellular medium was [Au] = 200 × 10^{-6} M. Following nanoparticle incubation, the cells were washed and detached to form the spheroids. The cells were then counted and divided into suspensions of 200 000 to 300 000 cells in 1.5 mL-Eppendorf tubes. The suspensions were subjected to centrifugation at 1,000 rpm for 5 min, resulting in the formation of cell pellets. These pellets were incubated at 37 °C with 5% CO_2 for a period of 2 days, allowing spherical aggregates to develop. Following this incubation, the aggregates were immobilized by treatment with a 4% paraformaldehyde (PFA) solution for 30 min, followed by three subsequent washes using phosphate-buffered saline (PBS). Finally, the aggregates were stored in PBS for further analysis.

Transmission Electron Microscopy (TEM): TEM micrographs of samples in aqueous dispersions and inside cells were captured using a JEM1400 Flash (Jeol) transmission electron microscope, operated at 120 kV, at the transmission electron microscopy service of CBM-CSIC, Spain. Sections of tumor cells labeled with nanoparticles were also prepared in the same service. Both control and labeled cells underwent washing and fixation with a suspension of 4% paraformaldehyde (PFA) and 2% glutaraldehyde in 0.1 mol L^{-1} sodium cacodylate buffer (pH 7.4) for 2 h. Subsequently, they were gradually dehydrated in ethanol (30% to 100%) and stained with 1% osmium tetroxide containing 1.5% potassium cyanoferrate. The samples were then embedded in epoxy resin, cut with a microtome into sections, and mounted on grids for analysis.

X-Ray Diffraction (XRD): X-ray diffraction data were obtained at the Diffraction Facility of ICMM-CSIC, Madrid, Spain. Samples were placed on a glass slide and submerged in mineral oil. Suitable samples (Au nanoparticles-labeled cells) were selected with a kapton loop from MiTeGen, using a polarized optical microscope. Diffraction data was collected using Cu radiation with a Bruker D8 Venture diffractometer, equipped with three microsources (Cu, Mo, Ag) and a PHOTON III area detector. Data collection was performed with APEX5 software. DIFFRAC EVA software was used to obtain 1D XRD patterns.

Quantitative Elemental Analysis and Intracellular Uptake (ICP-OES): The concentration of Au in both solution and cells was determined using inductively coupled plasma optical emission spectrometry (ICP-OES) at the chemical analysis service of ICMM-CSIC, Spain, with an Optima 2100 DV PerkinElmer instrument. Nanoparticle solutions were prepared by adding 1 mL of aqua regia (a mixture of HNO_3:HCl in a 1:3 ratio) and heating them to 80 °C for 2 h. The sample was diluted in MilliQ water to achieve a final volume of 10 mL. Quantitative analysis of the elements was conducted using standard references for Au.

Optical Absorption Spectroscopy: The absorption spectra were recorded for aqueous suspensions and cells using a Cary 60 UV–Vis-NIR spectrometer (Varian) in the 300–1100 nm spectral range. Preparation of a cell lysate was performed to isolate endosomes from cell nuclei. The cells were suspended in a lysis buffer containing 250 mM sucrose and 3 mM imidazole. To enhance the release of labeled endosomes, mechanical disruption was induced using a needle syringe.

Photothermal Excitation Measurements: To assess temperature profiles, the labeled aggregates (3-4) were subjected to an 808 nm laser with a maximum power output of 1 W (Roithner Lasertechnik GmbH, Austria). The laser intensity was adjusted to 0.05, 0.15, 0.3, and 0.6 W. Measurements were taken after 10–15 min of irradiation, once the temperature stabilized, using an infrared thermal camera (FLIR, USA) to monitor the thermal increase.

Synchrotron hard X-Ray Absorption Spectroscopy (XAS): XAS spectra were recorded in fluorescence mode at the SAMBA beamline (SOLEIL synchrotron, France) using a multi-element high purity Germanium detector (HPGe, Mirion). Samples with AuNS were measured in multicellular aggregates (3-4) and deposited on Kapton films mounted on standard supports in a motorized stage. Spectra were acquired at the Au L_3-edge (11919 eV) across XANES and EXAFS regions. A liquid helium-nitrogen cryostat with vacuum/He-gas insulation enabled measurements from 100 to 350 K for calibration. An Au metallic foil was measured at every condition for energy calibration. Data were processed with Athena software, included in the Demeter system, for polynomial pre- and post-edge background subtraction. EXAFS fits were performed on the k^2-weighted signal Fourier-transformed in the 2.5–11.5 $Å^{-1}$ range, obtaining the radial distribution ≈ 1.0–5.0 Å from absorbing atoms (Au). Analysis calculations were conducted using Artemis software.[62]

Viability Assays of Cells and of Photoirradiated Spheroids: U87 cells were cultured in 24-well plates for 24 h with increasing concentrations of gold nanostars (ranging from 12.5 to 100 μg mL^{-1}) in a complete DMEM culture medium. Cell viability was assessed by a colorimetric method based on a resazurin solution assay. A 10% resazurin solution was added to the DMEM medium without red phenol and incubated for 2–3 h, then transferred to a 96-well plate. Fluorescence was analyzed by a microplate reader (excitation 570 nm, emission 585 nm, Bio-Tek instruments, Inc). Viability was normalized with unlabeled control cells.

The thermal damage effect after applying the photothermal treatments was evaluated in labeled spheroids subjected to different 808 nm power densities of laser. The spheroids were then immersed in a 10% Alamar Blue solution in DMEM without red phenol, incubated for 2 h. Metabolic activity was obtained by fluorescence analysis of the transferred solution

in a microplate reader. All reported experimental results were performed in triplicate. A thermostated device was used to ensure physiological temperature conditions (37 °C).

Alternatively, the cell survival was assessed with live/dead assay (LIVE/DEAD^{TM} Cell Imaging Kit Invitrogen R37601). The solution was prepared according to manufacturer's guidelines and the spheroids were incubated with it for 25 min at 37 °C, 5% CO_2. Confocal microscopy (Leica DMi8) was performed with × 25 magnification lens in water-immersion mode. The resulting images were obtained as 3D images (z-stacks, step size 2.0 µm, image size 1024 × 1024, resolution 2.2 pixels per micron) with two channels: Calcein Green & Texas Red, identifying live and dead signal respectively.

Immunofluorescence Staining of Photothermal Irradiated Spheroids: Following the laser exposure, spheroids were fixed with 4% paraformaldehyde for 1 h at room temperature, followed by three washes with PBS. They were then permeabilized with 0.1% Triton X-100 in PBS for 15 min at room temperature followed by blocking in a 2% bovine serum albumin (BSA), 0/1% Triton X-100 solution in PBS for 3 h at ambient temperature. Spheroids were then incubated with anti-E-cadherin primary antibody solution (Invitrogen SHE78-7) at 1:400 dilution in blocking solution overnight at room temperature. The next day, the samples were thoroughly rinsed 3x times with PBS and incubated with Alexa Fluor 488-conjugated goat anti-mouse IgG (H+L) highly cross-adsorbed secondary antibody, (ThermoFisher A11029) at 1:400 in blocking solution overnight at room temperature. Finally, following 3x washings with PBS, spheroids were incubated in a 300 nM DAPI solution (D3571, Invitrogen) at a 1:500 dilution with Alexa Fluor 555 Phalloidin (Thermofisher A34055) at 1:1000 in blocking solution at room temperature overnight. Lastly, spheroids were rinsed with PBS 3x times before acquiring images. Imaging was performed in z-stack sections with Leica DMi8 inverted confocal microscope (Leica Microsystems) using a 40x water immersion objective with voxel size of $0.2841 \times 0.2841 \times 0.7\ \mu m^3$.

Supporting Information

Supporting Information is available from the Wiley Online Library or from the author.

Acknowledgements

This work was funded by MCIN/AEI/10.13039/501100011033 (PID2021-127033OB-C21 (A. E.), PID2021-126323OA-I00 (A. M-N), PID2022-139467OB-I00 (J. R.), PID2020-114192RB-C41 (M. A. G.)), MCIU/AEI/10.13039/501100011033 and the European Union NextGenerationEU/PRTR (CNS2023-144689 (A. E.), CNS2023-144128 (A.M-N.), CNS2023-144447 (J. R.)), the European Union (ERC-2019-CoG project NanoBioMade 865629 (C. W.)), CSIC (PIE-20226AT024 (A. E.)) and Programa de Ayudas I+ D en Biomedicina de la Comunidad de Madrid (ASAP-CM S2022/BMD-7434). IMDEA Nanociencia acknowledges support from the Severo Ochoa program for Centers of Excellence in R&D (CEX2020-001039-S) and FPI grant PRE2020-96246 (R. L-M.). The authors thank Milagros Guerra for TEM sample preparation at the Electron Microscopy Service of the Centro de Biología Molecular Severo Ochoa (CBM, CSIC-UAM, Spain), the technical staff at ICMM-CSIC for ICP-OES measurements, and the Histology Facility at CNB-CSIC (Spain) for histological preparation of biological samples. The authors also thank the SAMBA beamline staff at SOLEIL Synchrotron (France) for their support during experiments. Finally, the authors acknowledge the Conexión Nanomedicina network from CSIC, Spain.

Conflict of Interest

The authors declare no conflict of interest.

Data Availability Statement

The data that support the findings of this study are available from the corresponding author upon reasonable request.

Keywords

Nanomedicine, Nanothermal therapy, Nanothermometry, Photothermia, Plasmonic nanoparticles, X-ray absorption spectroscopy

Received: October 3, 2024
Revised: November 8, 2024
Published online:

[1] X. Huang, P. K. Jain, I. H. El-Sayed, M. A. El-Sayed, *Las. Med. Sci.* **2008**, *23*, 217.
[2] D. Jaque, L. M. Maestro, B. Del Rosal, P. Haro-Gonzalez, A. Benayas, J. Plaza, E. M. Rodriguez, J. G. Sole, *Nanoscale* **2014**, *6*, 9494.
[3] P. K. Jain, X. Huang, I. H. El-Sayed, M. A. El-Sayed, *Acc. Chem. Res.* **2008**, *41*, 1578.
[4] M. Rai, A. P. Ingle, S. Birla, A. Yadav, C. A. D. Santos, *Crit. Rev. Microbiol.* **2016**, *42*, 696.
[5] A. Espinosa, A. Curcio, S. Cabana, G. Radtke, M. Bugnet, J. Kolosnjaj-Tabi, C. Péchoux, C. Alvarez-Lorenzo, G. A. Botton, A. Silva, *ACS Nano* **2018**, *12*, 6523.
[6] B. Han, Y. L. Zhang, Q. D. Chen, H. B. Sun, *Adv. Funct. Mater.* **2018**, *28*, 1802235.
[7] L. Đorđević, F. Arcudi, M. Cacioppo, M. Prato, *Nat. Nanotechnol.* **2022**, *17*, 112.
[8] I. Marangon, C. Ménard-Moyon, A. K. Silva, A. Bianco, N. Luciani, F. Gazeau, *Carbon* **2016**, *97*, 110.
[9] M. P. Romero, H. H. Buzza, M. D. Stringasci, B. M. Estevão, C. C. Silva, M. A. Pereira-da-Silva, N. M. Inada, V. S. Bagnato, *Int. J. Nanomed.* **2021**, 1601.
[10] Y. Shen, H. D. Santos, E. C. Ximendes, J. Lifante, A. Sanz-Portilla, L. Monge, N. Fernandez, I. Chaves-Coira, C. Jacinto, C. D. Brites, L. D. Carlos, A. Benayas, M. Carmen Iglesias-de la Cruz, D. Jaque, *Adv. Funct. Mater.* **2020**, *30*, 2002730.
[11] R. Marin, A. Skripka, L. V. Besteiro, A. Benayas, Z. Wang, A. O. Govorov, P. Canton, F. Vetrone, *Small* **2018**, *14*, 1803282.
[12] A. Curcio, A. K. Silva, S. Cabana, A. Espinosa, B. Baptiste, N. Menguy, C. Wilhelm, A. Abou-Hassan, *Theranostics* **2019**, *9*, 1288.
[13] A. Espinosa, R. Di Corato, J. Kolosnjaj-Tabi, P. Flaud, T. Pellegrino, C. Wilhelm, *ACS Nano* **2016**, *10*, 2436.
[14] A. Espinosa, J. Kolosnjaj-Tabi, A. Abou-Hassan, A. Plan Sangnier, A. Curcio, A. K. Silva, R. Di Corato, S. Neveu, T. Pellegrino, L. M. Liz-Marzán, *Adv. Funct. Mater.* **2018**, *28*, 1803660.
[15] D. Xu, Z. Li, L. Li, J. Wang, *Adv. Funct. Mater.* **2020**, *30*, 2000712.
[16] R. Bardhan, S. Lal, A. Joshi, N. J. Halas, *Acc. Chem. Res.* **2011**, *44*, 936.
[17] J. Hu, F. Sanz-Rodríguez, F. Rivero, E. M. Rodríguez, R. A. Torres, D. H. Ortgies, J. G. Solé, F. Alfonso, D. Jaque, *Nano Res.* **2017**, *11*, 676.
[18] X. Huang, I. H. El-Sayed, W. Qian, M. A. El-Sayed, *J. Am. Chem. Soc.* **2006**, *128*, 2115.
[19] R. n. Ahijado-Guzmán, G. González-Rubio, J. s. G. Izquierdo, L. Bañares, I. n. López-Montero, A. Calzado-Martín, M. Calleja, G. Tardajos, A. s. Guerrero-Martínez, *ACS Omega* **2016**, *1*, 388.
[20] J. Chen, C. Glaus, R. Laforest, Q. Zhang, M. Yang, M. Gidding, M. J. Welch, Y. Xia, *Small* **2010**, *6*, 811.
[21] W. Lu, C. Xiong, G. Zhang, Q. Huang, R. Zhang, J. Z. Zhang, C. Li, *Clin. Cancer Res.* **2009**, *15*, 876.

[22] A. M. Goodman, Y. Cao, C. Urban, O. Neumann, C. Ayala-Orozco, M. W. Knight, A. Joshi, P. Nordlander, N. J. Halas, *ACS Nano* **2014**, *8*, 3222.
[23] S. K. Dondapati, T. K. Sau, C. Hrelescu, T. A. Klar, F. D. Stefani, J. Feldmann, *ACS Nano* **2010**, *4*, 6318.
[24] H. Yuan, C. G. Khoury, C. M. Wilson, G. A. Grant, A. J. Bennett, T. Vo-Dinh, *Nanomed.: Nanotechnol., Biol. Med.* **2012**, *8*, 1355.
[25] F. Tian, J. Conde, C. Bao, Y. Chen, J. Curtin, D. Cui, *Biomaterials* **2016**, *106*, 87.
[26] L. Rodríguez-Lorenzo, R. de La Rica, R. A. Álvarez-Puebla, L. M. Liz-Marzán, M. M. Stevens, *Nat. Mater.* **2012**, *11*, 604.
[27] A. Espinosa, A. K. Silva, A. Sánchez-Iglesias, M. Grzelczak, C. Péchoux, K. Desboeufs, L. M. Liz-Marzán, C. Wilhelm, *Adv. Healthcare Mater.* **2016**, *5*, 1040.
[28] S. Barbosa, A. Agrawal, L. Rodríguez-Lorenzo, I. Pastoriza-Santos, R. A. Alvarez-Puebla, A. Kornowski, H. Weller, L. M. Liz-Marzán, *Langmuir* **2010**, *26*, 14943.
[29] H. Chatterjee, D. S. Rahman, M. Sengupta, S. K. Ghosh, *J. Phys. Chem. C* **2018**, *122*, 13082.
[30] H. Wang, X. Liu, X. Li, W. Lu, L. Jiang, *ChemistrySelect* **2016**, *1*, 659.
[31] K. Chandra, K. S. Culver, S. E. Werner, R. C. Lee, T. W. Odom, *Chem. Mater.* **2016**, *28*, 6763.
[32] H. Tan, N. Hou, Y. Liu, B. Liu, W. Cao, D. Zheng, W. Li, Y. Liu, B. Xu, Z. Wang, *Nanomed.: Nanotechnol., Biol. Med.* **2020**, *27*, 102192.
[33] D. Wu, P. Zhao, L. Wu, L. Lin, G. Yu, L. Xu, J. Yue, *ACS Appl. Bio Mater.* **2020**, *3*, 4590.
[34] D. Miao, Y. Yu, Y. Chen, Y. Liu, G. Su, *Mol. Pharmaceutics* **2020**, *17*, 1127.
[35] S. Wang, P. Huang, L. Nie, R. Xing, D. Liu, Z. Wang, J. Lin, S. Chen, G. Niu, G. Lu, *Adv. Mater.* **2013**, *25*, 3055.
[36] L. Zhang, X.-Q. Yang, J.-S. Wei, X. Li, H. Wang, Y.-D. Zhao, *Theranostics* **2019**, *9*, 5424.
[37] Z. Li, F. Yang, D. Wu, Y. Liu, Y. Gao, H. Lian, H. Zhang, Z. Yin, A. Wu, L. Zeng, *Nanoscale* **2020**, *12*, 22173.
[38] M. P. Ogáyar, R. López-Méndez, I. Figueruelo-Campanero, T. Muñoz-Ortiz, C. Wilhelm, D. Jaque, A. Espinosa, A. Serrano, *Nanoscale Adv.* **2024**, *6*, 4635.
[39] D. Jaque, F. Vetrone, L. nanothermometry, *Nanoscale* **2012**, *4*, 4301.
[40] J. G. Ovejero, I. Armenia, D. Serantes, S. Veintemillas-Verdaguer, N. Zeballos, F. López-Gallego, C. Grüttner, J. M. de la Fuente, M. a. d. Puerto Morales, V. Grazu, *Nano Lett.* **2021**, *21*, 7213.
[41] D. Ruiz, B. del Rosal, M. Acebrón, C. Palencia, C. Sun, J. Cabanillas-González, M. López-Haro, A. B. Hungría, D. Jaque, B. H. Juarez, *Adv. Funct. Mater.* **2017**, *27*, 1604629.
[42] P. Haro-González, L. Martínez-Maestro, I. Martín, J. García-Solé, D. Jaque, *Small* **2012**, *8*, 2652.
[43] P. Neumann, I. Jakobi, F. Dolde, C. Burk, R. Reuter, G. Waldherr, J. Honert, T. Wolf, A. Brunner, J. H. Shim, *Nano Lett.* **2013**, *13*, 2738.
[44] A. Riedinger, P. Guardia, A. Curcio, M. A. Garcia, R. Cingolani, L. Manna, T. Pellegrino, *Nano Lett.* **2013**, *13*, 2399.
[45] J. T. Dias, M. Moros, P. del Pino, S. Rivera, V. Grazú, J. M. de la Fuente, *Angew. Chem., Int. Ed.* **2013**, *52*, 11526.
[46] Y. Zhang, J. Yu, D. J. Birch, Y. Chen, *J. Biomed. Opt.* **2010**, *15*, 020504.
[47] B. Van de Broek, D. Grandjean, J. Trekker, J. Ye, K. Verstreken, G. Maes, G. Borghs, S. Nikitenko, L. Lagae, C. Bartic, *Small* **2011**, *7*, 2498.
[48] A. Espinosa, G. R. Castro, J. Reguera, C. Castellano, J. Castillo, J. Camarero, C. Wilhelm, M. A. García, A. I. Muñoz-Noval, *Nano Lett.* **2021**, *21*, 769.
[49] R. López-Méndez, J. Reguera, A. Fromain, E. S. Abu Serea, E. Céspedes, F. Terán, F. Zheng, A. Parente, M. Á. García, E. Fonda, C. Wilhelm, J. Camarero, A. I. Muñoz-Noval, A. Espinosa, *Adv. Health. Mater.* **2023**, *12*, 2301863.
[50] R. Gupta, D. Sharma, *Nanoscale Adv.* **2021**, *3*, 3663.
[51] K. M. Yamada, E. Cukierman, *Cell* **2007**, *130*, 601.
[52] S. C. Brüningk, I. Rivens, C. Box, U. Oelfke, G. Ter Haar, *Sci. Rep.* **2020**, *10*, 1653.
[53] L. Beola, L. Asín, R. M. Fratila, V. Herrero, J. M. De La Fuente, V. Grazú, L. Gutiérrez, *ACS Appl. Mater. Inter.* **2018**, *10*, 44301.
[54] M. Quintanilla, I. García, I. de Lázaro, R. García-Alvarez, M. Henriksen-Lacey, S. Vranic, K. Kostarelos, L. M. Liz-Marzán, *Theranostics* **2019**, *9*, 7298.
[55] A. Fromain, J. E. Perez, A. Van de Walle, Y. Lalatonne, C. Wilhelm, *Nat. Commun.* **2023**, *14*, 4637.
[56] M. Nabil, P. Decuzzi, P. Zunino, *R. Soc. Open Sci.* **2015**, *2*, 150447.
[57] J. Liu, L. Kang, I. Ratnayake, P. Ahrenkiel, S. Smith, C. Wang, *J. Colloid Interface Sci.* **2021**, *601*, 556.
[58] A. C. Daulagala, M. C. Bridges, A. Kourtidis, *Int. J. Mol. Sci.* **2019**, *20*, 2756.
[59] J. E. Perez, I. Nagle, C. Wilhelm, *Biofabrication* **2020**, *13*, 015018.
[60] D. J. Rosen, S. Yang, E. Marino, Z. Jiang, C. B. Murray, *J. Phys. Chem. C* **2022**, *126*, 3623.
[61] J. J. Rehr, R. C. Albers, *Rev. Modern Phys.* **2000**, *72*, 621.
[62] B. Ravel, M. Newville, A. R. T. E. M. I. S. ATHENA, *J. Synchrotron Radiat.* **2005**, *12*, 537.
[63] E. M. Scutigliani, Y. Liang, H. Crezee, R. Kanaar, P. M. Krawczyk, *Cancers* **2021**, *13*, 1243.
[64] T. Zhou, M. Yu, B. Zhang, L. Wang, X. Wu, H. Zhou, Y. Du, J. Hao, Y. Tu, C. Chen, *Adv. Funct. Mater.* **2014**, *24*, 6922.
[65] J. Dong, J. I. Zink, *ACS Nano* **2014**, *8*, 5199.
[66] S. Rohani, M. Quintanilla, S. Tuccio, F. De Angelis, E. Cantelar, A. O. Govorov, L. Razzari, F. Vetrone, *Adv. Opt. Mater.* **2015**, *3*, 1606.
[67] K. Nigoghossian, S. Ouellet, J. Plain, Y. Messaddeq, D. Boudreau, S. J. Ribeiro, *J. Mater. Chem. B* **2017**, *5*, 7109.
[68] M. L. Debasu, D. Ananias, I. Pastoriza-Santos, L. M. Liz-Marzán, J. Rocha, L. D. Carlos, *Adv. Mater.* **2013**, *25*, 4868.
[69] L. M. Machesky, *FEBS Lett.* **2008**, *582*, 2102.
[70] X. Li, J. Wang, *Int. J. Biol. Sci.* **2020**, *16*, 2014.
[71] C. M. Fife, J. A. McCarroll, M. Kavallaris, *Br. J. Pharmacol.* **2014**, *171*, 5507.
[72] J. M. Peng, R. Bera, C. Y. Chiou, M. C. Yu, T. C. Chen, C. W. Chen, T. R. Wang, W. L. Chiang, S. P. Chai, Y. Wei, *Hepatology* **2018**, *67*, 2226.
[73] M. R. Ali, Y. Wu, Y. Tang, H. Xiao, K. Chen, T. Han, N. Fang, R. Wu, M. A. El-Sayed, *Proc. Natl. Acad. Sci. USA* **2017**, *114*, E5655.
[74] Y. Wu, M. R. Ali, B. Dong, T. Han, K. Chen, J. Chen, Y. Tang, N. Fang, F. Wang, M. A. El-Sayed, *ACS Nano* **2018**, *12*, 9279.
[75] X. Ma, R. Hartmann, D. Jimenez de Aberasturi, F. Yang, S. J. Soenen, B. B. Manshian, J. Franz, D. Valdeperez, B. Pelaz, N. Feliu, *ACS nano* **2017**, *11*, 7807.